The Astrophysical Journal, 812:119 (13pp), 2015 October 20 doi:10.1088/0004-637X/812/2/119

PHYSICAL CONDITIONS OF CORONAL PLASMA AT THE TRANSIT OF A SHOCK DRIVEN BY A CORONAL MASS EJECTION

R. Susino, A. Bemporad, and S. Mancuso
INAF–Turin Astrophysical Observatory, via Osservatorio 20, I-10025 Pino Torinese (TO), Italy; susino@oato.inaf.it
Received 2015 April 10; accepted 2015 August 15; published 2015 October 15

ABSTRACT

We report here on the determination of plasma physical parameters across a shock driven by a coronal mass ejection using white light (WL) coronagraphic images and radio dynamic spectra (RDS). The event analyzed here is the spectacular eruption that occurred on 2011 June 7, a fast CME followed by the ejection of columns of chromospheric plasma, part of them falling back to the solar surface, associated with a M2.5 flare and a type-II radio burst. Images acquired by the *Solar and Heliospheric Observatory*/LASCO coronagraphs (C2 and C3) were employed to track the CME-driven shock in the corona between 2–12 $R_\odot$ in an angular interval of about 110°. In this interval we derived two-dimensional (2D) maps of electron density, shock velocity, and shock compression ratio, and we measured the shock inclination angle with respect to the radial direction. Under plausible assumptions, these quantities were used to infer 2D maps of shock Mach number M_A and strength of coronal magnetic fields at the shock's heights. We found that in the early phases (2–4 $R_\odot$) the whole shock surface is super-Alfvénic, while later on (i.e., higher up) it becomes super-Alfvénic only at the nose. This is in agreement with the location for the source of the observed type-II burst, as inferred from RDS combined with the shock kinematic and coronal densities derived from WL. For the first time, a coronal shock is used to derive a 2D map of the coronal magnetic field strength over intervals of 10 $R_\odot$ altitude and ∼110° latitude.

Key words: methods: data analysis – shock waves – Sun: corona – Sun: coronal mass ejections (CMEs) – Sun: magnetic fields

1. INTRODUCTION

The study of interplanetary shocks associated with major solar eruptions is very important not only from the theoretical point of view, but also because of potential impacts on human technologies. First because shocks, as well as solar flares, are optimal locations for the acceleration of solar energetic particles (SEPs; i.e., electrons, protons, and He ions with energies from a few keV to some GeV) that constitute an important hazard for satellites and astronauts, and may affect the ionosphere around polar caps. Moreover, as the shocks reach the Earth, significant southward components of the interplanetary magnetic field associated with them can magnetically reconnect with the magnetosphere, thus disturbing the system and producing severe geomagnetic storms (see, e.g., the review by Schwenn 2006). Hence, understanding the origin, propagation, and physical properties of interplanetary shocks is also crucial for future developments of our capabilities of forecasting possible space weather effects of solar activity. For these reasons, over the last decades huge efforts have been devoted in order to improve our knowledge of these phenomena and of the associated coronal mass ejections (CMEs), by using different instrumentation taking remote sensing as well as in situ data. In particular, over the last few years, the most recent space-based missions, such as the twin *STEREO* satellites, the *Hinode* and *SDO* observatories, have provided significant new insights, thus allowing shocks to be investigated from the early phases of their formation at the base of the corona out to their propagation into interplanetary space.

A clear signature of the formation and propagation of interplanetary shocks associated with CME expansion and/or flare explosions is the detection of type-II radio bursts (see Vršnak & Cliver 2008, for a review of the problem of type-II sources). Combination of radio data with images acquired at different wavelengths is able to provide unique new information on these phenomena. Recently, combined analysis of EUV images and radio dynamic spectra (RDS) were used to demonstrate (Cho et al. 2013; Chen et al. 2014) that type-II bursts may be excited in the lower corona through interaction between CMEs and nearby dense structures such as streamers (see also Reiner et al. 2003; Mancuso & Raymond 2004; Classen & Aurass 2008). A similar result was also obtained with the use of a new radio triangulation technique exploiting radio data acquired by different spacecraft (Magdalenić et al. 2014). Hence, type-II radio bursts are likely to be excited during the early propagation phase of the shocks (that is, at heliocentric distances $r < 1.5\ R_\odot$), around the expected location of the local minimum of the $v_A(r)$ profile (Gopalswamy et al. 2012, 2013). Thanks to the high cadence, good sensitivity, and spatial resolution now available in EUV with *SDO*/AIA, it has been shown (Kouloumvakos et al. 2014) also that the sole analysis of EUV images can provide by itself an estimate of the density compression ratio X (an important shock parameter given by the ratio between the downstream and the upstream plasma densities, $X = n_d/n_u$) and that this estimate is in agreement with the one derived from radio data in sheath regions. The above results clearly have important implications for the identification of SEP source regions.

Over the last decade it also became clear that a significant amount of information on interplanetary shocks can be derived from white light (WL) coronagraph data alone, as first shown by Vourlidas et al. (2003). Analysis of these data allowed one to verify that shocks form when their propagation velocity v_{sh} (measured in a reference system at rest with respect to the solar wind, moving at velocity v_{sw}) is larger than the local Alfvén velocity v_A ($|\boldsymbol{v}_{sh} - \boldsymbol{v}_{sw}| > v_A = B/\sqrt{4\pi\rho}$). Hence, the lower the velocity of the driver, the larger the distances where the

shock front forms (Eselevich & Eselevich 2011). Moreover, combination of EUV and WL data shows that the shock thickness δ is of the same order as the proton mean free path λ_p only for heliocentric distances $r < 6\ R_\odot$, while higher up in the corona $\delta \ll \lambda_p$. Hence, during its propagation, the shock regime changes from collisional to collisionless (Eselevich & Eselevich 2012). These details are crucial for our understanding of the physics at the base of the shock. Also, at larger heliocentric distances, the analysis of WL data provided by heliospheric imagers has demonstrated that the driver (CME) and the shock undergo different magnetic drag deceleration during their interplanetary expansion, with the shock propagating faster than the ejecta, thus leading to possible CME–shock decouplings (Hess & Zhang 2014). Statistically, the coupling has been found to be stronger for faster CMEs (Mujiber Rahman et al. 2013). Studies of interplanetary propagation of shocks have tremendous implications for our capability to predict space weather as well.

Significant advances were also made from comparisons between observations and numerical simulations. At heliocentric distances $r > 2\ R_\odot$ coronal protons and electrons are no longer coupled by Coulomb collisions. This leads to different temperatures for these two species, with slightly larger proton than electron temperatures (by a factor depending on the relevant altitude and coronal structure) as demonstrated by coronal UV spectra acquired by the UV Coronagraph Spectrometer (UVCS; see reviews by Antonucci 2006; Kohl et al. 2006). Protons, however, being much heavier than electrons, have much smaller microscopic velocities (by a factor of 42.85). CME-driven shocks are thus supersonic only with respect to the proton thermal speed, implying that only protons are expected to be significantly heated by the transit of the shock. This was recently confirmed from both observations and simulations: in particular, Manchester et al. (2012) and Jin et al. (2013) demonstrate that the WL appearances of CME-driven shocks are better reproduced by two-temperature (2T) MHD simulations than one-temperature (1T) simulations, where 2T plasma protons are heated up to ~90 MK, and 2T shocks have larger Alfvénic Mach numbers M_A (by a factor ~1.25–1.4) than in the 1T plasma case. Very similar results were recently obtained by the combined analysis of UV and WL observations of a CME-driven shock performed by Bemporad et al. (2014).

The latter work was the result of a sequence of previous researches performed on CME-driven shocks and based on the combined analyses of UV spectra acquired by UVCS and WL images acquired by the LASCO coronagraph. As first demonstrated by Bemporad & Mancuso (2010), this unique combination allows one to measure not only the plasma compression ratio X, but also the pre- and post-shock plasma temperatures. Moreover, once this information is combined with the Rankine–Hugoniot equations written for the general case of oblique shocks, and by measuring geometrical (inclination) and kinematic (velocity) properties of the shock from WL data, it is even possible to determine both the pre- and post-shock magnetic and velocity field vectors projected on the plane of the sky. This technique allowed Bemporad & Mancuso (2011, 2013) to conclude that, for a few specific events, radio-loud (radio-quiet) CMEs are more likely associated with supercritical (subcritical) shocks, and that only a small region around the shock center is supercritical in the early evolution phases, while higher up (i.e., later on) the whole shock becomes subcritical. Moreover, the same technique applied to different points located along the same shock front allowed Bemporad et al. (2014) to demonstrate that the transit of the shock leads to a significant deflection of the magnetic field close to the shock nose, and a smaller deflection at the flanks, implying a draping of field lines around the expanding CME, in nice agreement with the post-shock magnetic field rotations obtained by Liu et al. (2011) with 3D MHD numerical simulations.

In this paper the above results are further extended: in particular we demonstrate here that, under some specific hypotheses, the analysis of WL coronagraphic data alone can provide not only the density compression ratios at different times and locations along the shock front, but also the M_A numbers and the pre-shock coronal magnetic fields, allowing us to derive a two-dimensional (2D) map of magnetic field strength covering a heliocentric distance interval of ~10 $R_\odot$ and a latitude interval of ~110°. Moreover, the combined analysis of WL and radio data allows us to derive the possible location of the source for the type-II radio burst. The paper is organized as follows: after a general description of the event being analyzed here (Section 2), we describe the analysis of data (Section 3), focusing in particular on LASCO/C2 and C3 WL coronagraphic images (Section 3.1) and WAVES/RAD1-RAD2 RDS (Section 3.2). Then, the obtained results are summarized and discussed (Section 4).

2. OBSERVATIONS

On 2011 June 7, a GOES M2.6 class flare from AR 11226 (located in the southwest quadrant at 22° S and 66° W) occurred between 06:16 and 06:59 UT, peaking around 06:16 UT. This soft X-ray flare was associated with significant HXR emission and even γ-ray emission lasting for about 2 hr (Ackermann et al. 2014). The impressive eruption associated with this flare has been extensively studied by many previous authors who focused on different physical phenomena related to the event. They focused on several aspects of this event, such as the early evolution of the released CME bubble and compression front (Cheng et al. 2012), the propagating EUV wave (Li et al. 2012), the magnetic reconnections driven by the CME expansion (van Driel-Gesztelyi et al. 2014), the flare emission (Inglis & Gilbert 2013), and the associated type-II radio burst (Dorovskyy et al. 2015). Moreover, this spectacular eruption was followed by the ejection of huge radial columns of chromospheric plasma, reaching the field of view of LASCO and COR1 coronagraphs, and then falling back to the Sun. Thus, other authors focused also on the dynamics and plasma properties of returning plasma blobs (Innes et al. 2012; Williams et al. 2013; Carlyle et al. 2014; Dolei et al. 2014), as well as on the energy released from the impact of material falling on the Sun (Gilbert et al. 2013; Reale et al. 2013, 2014).

In this work we study the evolution of the shock wave associated with this eruption as observed by WL coronagraphic images. As reported by Cheng et al. (2012), immediately after the flare onset (around 06:26 UT) a circular plasma CME bubble was observed in the *SDO*/AIA images expanding at ~960 km s^{-1}; in the early phases, due to the small standoff distance, the compression front and the front of the driver (i.e., the CME bubble) cannot be discerned. The two fronts started to separate only later on, when a deceleration of the CME bubble is observed; at the same time, a type-II radio burst started (as well as a type-III burst), suggesting that the compression wave had just turned itself into a shock wave. Later on, the CME

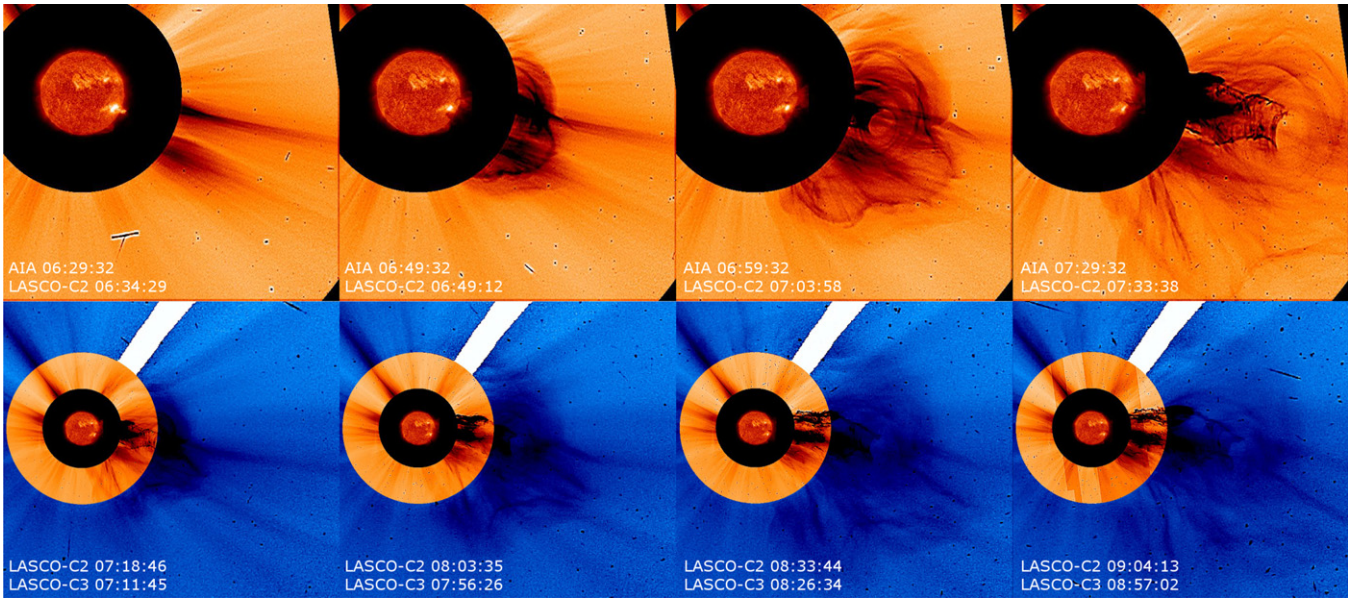

Figure 1. Top: sequence of *SDO*/AIA 304 and *SOHO*/LASCO C2 images acquired on 2011 June 7, during the eruptive event analyzed here. The LASCO C2 images are shown in inverted color scale (brighter features are darker and vice versa) and after the application of a filter to enhance the visibility of CME structures (images created with JHelioviewer). Bottom: sequence of LASCO C2 and C3 images showing the CME propagation at higher altitudes; again the images are shown in inverted color scale and after the application of a filter to enhance the visibility of CME structures (images created with JHelioviewer).

enters the field of view of the *Solar and Heliospheric Observatory* (*SOHO*)/LASCO C2 coronagraph, starting from the frame acquired at 06:49 UT (Figure 1, top row), and then enters the field of view of the LASCO C3 coronagraph, starting from the frame acquired at 07:11 UT (Figure 1, bottom row). The LASCO C2 frames clearly show the propagation of the shock wave associated with the event, as well as the CME front and the circular flux rope, while this latter part becomes hardly discernible in the LASCO C3 frames (see Figure 1).

In what follows we describe how the sequence of WL images acquired by LASCO C2 and C3 has been analyzed to derive the pre-CME coronal density and the different physical parameters of the shock wave.

3. DATA ANALYSIS

3.1. WL Coronagraphic Images

3.1.1. Pre-CME Coronal Densities

For the density calculation we use *SOHO*/LASCO C2 polarized brightness (pB) images. It is well known that the K-corona brightness originates from Thomson scattering of photospheric light by free electrons in the solar corona (e.g., Billings 1966). Because the emission is optically thin, the observer sees a contribution from electrons located all along the line of sight. In addition to the K-corona, observations will contain a component due to scattering of photospheric light from interplanetary dust (the so-called F-corona). This component must be eliminated from the data to derive the coronal electron density; however, in the case of pB observations at small altitudes ($\lesssim 5\ R_\odot$), the F-corona can be assumed to be unpolarized and thus does not contribute to the pB (Hayes et al. 2001).

The intensity of the scattered light depends on the number of scattering electrons and several geometric factors, as was first shown by Minnaert (1930). In the absence of an F-corona, the pB observed on the plane of the sky is given by the following equation:

$$\mathrm{pB}(\varrho) = C \int_{\varrho}^{\infty} n_{\mathrm{e}}(r)[A(r) - B(r)] \frac{\varrho^2\, dr}{r\sqrt{r^2 - \varrho^2}}, \qquad (1)$$

where C is a unit conversion factor, n_{e} is the electron density, A and B are geometric factors (van de Hulst 1950; Billings 1966), ϱ is the projected heliocentric distance of the point (impact distance), and r is the actual heliocentric distance from center of the Sun. The integration is performed along the line of sight through the considered point. van de Hulst (1950) developed a well known method for estimating the electron density by the inversion of Equation (1) under the assumptions that: (1) the observed pB along a single radial direction can be expressed in the polynomial form $\mathrm{pB}(r) = \sum_k \alpha_k r^{-k}$ and (2) that the coronal electron density is axisymmetric. We apply this method to the latest LASCO C2 pB image acquired before the June 7 CME, in order to determine the pre-CME electron density distribution in the corona.

The pB image considered here is obtained from the polarization sequence of observations recorded on 2011 June 4, starting at 02:54 UT, i.e., about three days before the occurrence of the June 7 CME. During this three-day time lag, three other much smaller CMEs occurred with a central propagation direction in the same latitudinal sector crossed by the June 7 CME (70° S–40° N), as reported in the *SOHO*/LASCO CME catalog: on June 4, at 06:48 UT and 22:05 UT, and on June 6, at 07:30 UT. Nevertheless, despite these smaller scale events and coronal evolution, a direct comparison between the LASCO C2 WL images acquired on June 4 at 02:48 UT and on June 7 immediately before the eruption at 06:04 UT shows that the overall density structure of the corona above the west limb of the Sun is quite similar even after more than three days (Figure 2), hence the electron density estimated from the inversion of the June 4 pB data can be considered at

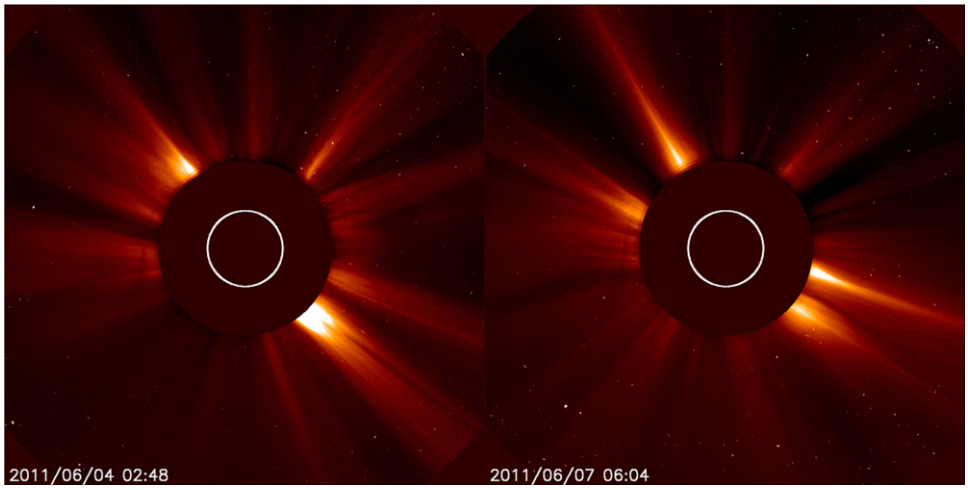

Figure 2. Appearance of the white light corona as observed on June 4, 02:48 UT (left) before the acquisition of the pB image used for the coronal density determination, and on June 7, 06:04 UT (right) before the occurrence of the eruption.

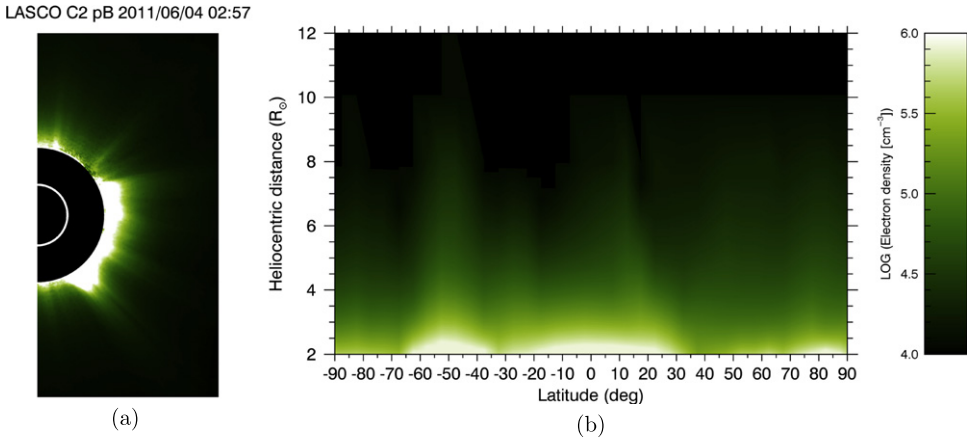

Figure 3. LASCO C2 polarized brightness image of the solar corona above the west limb, acquired on 2011 June 4 at 02:57 UT (a) and the corresponding 2D electron density map derived from the inversion of the pB data (b).

least a first-order approximation of the real pre-CME coronal density configuration.

The radial profiles of electron density obtained at different latitudes from the pB image (Figure 3(a)) are combined into a 2D map in polar coordinates, shown in Figure 3(b). The map shows the density distribution in the latitudinal region being crossed later on by the shock, for heliocentric distances ranging between 2 and 12 $R_{\odot}$; electron densities at distances from the Sun larger than 6 $R_{\odot}$ (the outer limit of the LASCO C2 field of view) are obtained through a power-law extrapolation of the density profiles assuming a radial dependence proportional to r^{-2}. The presence of the coronal streamer centered around 50° S, which persists till June 7, is very clear as it is associated with a local electron density maximum. Notice that, in general, coronal features are much less evident in the pB image and in the density map (Figure 3) than in the regular LASCO frames (Figure 2) because the latter are obtained after subtraction of a monthly minimum background average to enhance the visibility of fainter structures.

3.1.2. Shock Position and Kinematics

WL coronagraphic images can be used to identify the shock front location at different times and to distinguish between the shock-compressed plasma and the CME material, as extensively demonstrated by several works (e.g., Vourlidas et al. 2003; Ontiveros & Vourlidas 2009; Bemporad & Mancuso 2010, 2011). The CME-driven shock front can be identified as a weak increase in brightness located above the expanding CME front, which is generally interpreted as the visible signature of the downstream plasma compression and density enhancement caused by the transit of the shock; for this reason, the shock front becomes visible only when the intensity scale of WL images is adjusted to bring out the fainter structures.

In this work, we determine the location of the shock front in both LASCO C2 and C3 total brightness images using a common procedure that consists of three steps: (1) we compute excess-mass (or base-difference) images by subtracting from each calibrated LASCO frame an average pre-event image that is representative of the quiescent background corona (see Vourlidas et al. 2000; Ontiveros & Vourlidas 2009); (2) we apply a normalizing radial graded filter (NRGF), as described by Morgan et al. (2006), in order to reveal faint emission features at high heliocentric distances in the corona (this is particularly useful for the identification of the shock front in LASCO C3 images); (3) we measure the projected altitude of the shock by locating the intensity jump at the front in the radial direction. With this technique the location of the shock

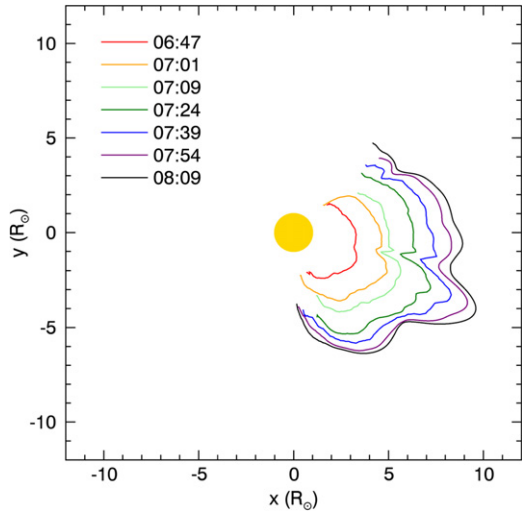

Figure 4. Cartesian plot showing the locations of the shock front identified at different times in LASCO C2 and C3 white-light images.

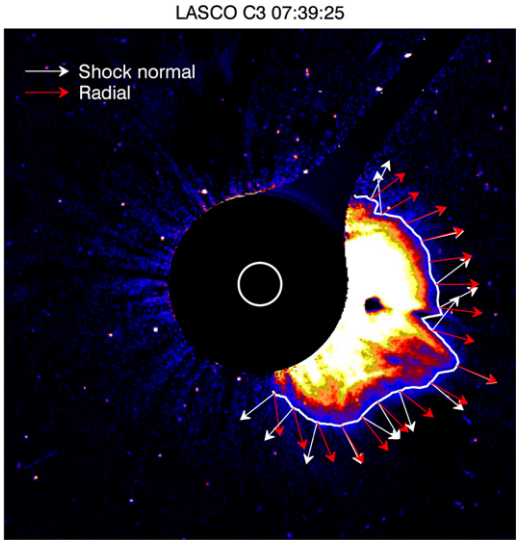

Figure 5. Base-difference LASCO C3 image showing the location of the shock front (solid white line) at 07:39 UT and a schematic representation of selected vectors normal to the shock surface (white arrows) and corresponding radial directions in the same points (red arrows).

can be identified with an estimated uncertainty of ±3 pixels on average and ±5 pixels for LASCO C2 and C3 images. Larger uncertainties could be related to the applied procedure of background subtraction, at the possible locations where the pre-eruption corona significantly changed during the event.

We apply this procedure to seven consecutive images where we could identify signatures of the shock: two from LASCO C2, acquired at 06:47 and 07:01 UT, and five from LASCO C3, acquired at 07:09, 07:24, 07:39, 07:54, and 08:09 UT (see Figure 1). Later on, we were not able to locate the shock front with a significant accuracy in LASCO C3 images. The curves giving the position of the shock fronts identified in the considered WL images are plotted in Figure 4. The shock appears to propagate almost symmetrically and to exhibit only a moderate latitudinal displacement, since the center of the shock (i.e., the highest point along the front) has a latitudinal location that is always in the range 21°–25° S. We notice here that around a latitude of about 12° S the identified location of the shock surface shows a clear discontinuity, which is likely due to the northward displacement of a pre-event coronal streamer, leading to an overestimate (underestimate) of the shock-projected altitude northward (southward) of the streamer itself.

These curves can be easily employed to derive, along the whole of each shock front, the angle θ_{sh} between the normal to the shock front and the radial direction, as well as the latitudinal distribution of the average shock speed, v_{sh}. These quantities are essential for the determination of the Alfvénic Mach number and the upstream plasma velocity distribution, as discussed in the following section. As an example, Figure 5 shows the relative orientation of vectors parallel with the radial direction and those normal to the shock surface at different positions along the front as we identified in the LASCO C3 image acquired at 07:39 UT. It is evident from this figure that θ_{sh} angles are in general larger at the flanks of the shock and smaller near the shock center (or "nose"). This result confirms what we already found in recent works (see, e.g., Bemporad et al. 2014) and suggests that we may expect the prevalence of quasi-perpendicular shock conditions at the flanks and quasi-parallel shock conditions at the center of the shock.

The radial component of the average shock speed is obtained at each latitude simply as $v_r = \Delta\varrho/\Delta t$, where $\Delta\varrho$ is the variation of the projected heliocentric distance of the shock measured in the radial direction between two consecutive shock curves. The true shock velocity can be then derived simply as $v_{sh} = v_r \cdot \cos\theta_{sh}$. Note that, as in Bemporad et al. (2014), this corresponds to assuming isotropic self-similar expansion of the front in the range of common latitudes between consecutive curves, but taking into account the correction for the latitudinal shock propagation. A 2D polar map of radial velocity distribution v_r in the region where the shock propagates is obtained by interpolating with polynomial fitting the heliocentric distance values at each latitude and altitude along the shock fronts, and is shown in Figure 7 (top-left panel). The resulting radial shock speed is (as expected) larger at the center of the shock at all altitudes, then it decreases toward the shock flanks; at a heliocentric distance of 2.5 $R_\odot$ it reaches a value as high as $\sim$1200 km s^{-1} near the center and $\sim$800–900 km s^{-1} about 20° away from it. The shock also appears to decelerate during its propagation, since the velocity at higher altitudes is progressively smaller: for instance, at 12 $R_\odot$ $v_{sh} \simeq$ 1000 km s^{-1} at the shock center. This means that the shock is losing its energy as it expands; this is also supported by the results we obtain for the compression ratio and the Alfvénic Mach number, as discussed in the following section.

3.1.3. Compression Ratio, Alfvénic Mach Number, and Alfvén Speed

The shock compression ratio X, defined as the ratio between the downstream (i.e., post-shock) and the upstream (i.e., pre-shock) plasma densities, $X \equiv \rho_d/\rho_u$, is determined here as described in Bemporad & Mancuso (2011). For each pixel along an identified shock front, we measure the total white-light brightness of the compressed downstream plasma, tB_d, from the corresponding LASCO C2 or C3 image, and, at the same locations in the corona, the upstream brightness tB_u from the last image acquired before the arrival of the shock. This provides us with the observed ratio $(tB_d/tB_u)_{obs}$.

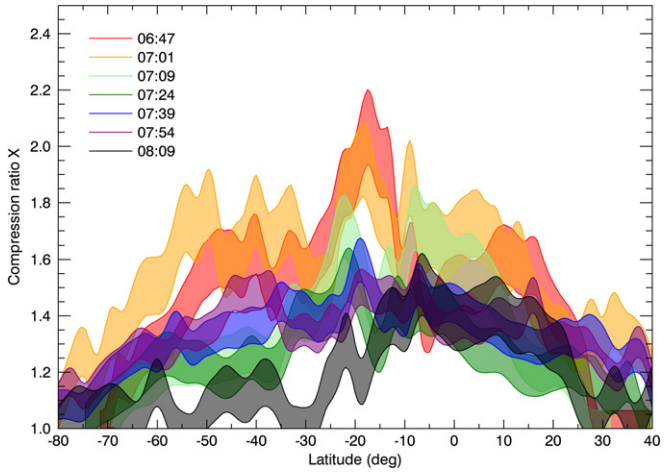

Figure 6. Compression ratios $X \equiv \rho_d/\rho_u$ as measured along the shock fronts identified in LASCO observations and reported in Figure 4. Each profile is shown as a thick shaded area representing the uncertainty in the derived X values.

On the other hand, the upstream total brightness $tB_u(\varrho)$ expected at a projected altitude ϱ in the corona can be evaluated through the line-of-sight integration of the upstream electron density profile, $n_e(r)$, multiplied by a geometrical factor K that includes all the geometrical parameters for Thomson scattering:

$$tB_u(\varrho) = \int_{\varrho}^{\infty} K(r, \varrho) \cdot n_e(r)\, dr, \tag{2}$$

where r is the heliocentric distance of the scattering point along the line of sight. The expected downstream total brightness tB_d is similarly given by the sum of two integrals: one performed over the unshocked corona (with density n_e) and the other over a length L across the shocked plasma with density $X \cdot n_e$ ($X \geqslant 1$):

$$\begin{aligned} tB_d(\varrho) \;=\; & \int_{\varrho}^{\infty} K(r, \varrho) \cdot n_e(r)\, dr \\ & + \int_{\varrho}^{r_{sh}} K(r, \varrho) \cdot (X - 1) \cdot n_e(r)\, dr, \end{aligned} \tag{3}$$

where $r_{sh} = \sqrt{\varrho^2 + L^2}$ and X is precisely the unknown compression ratio. The shock depth L is estimated as in Bemporad & Mancuso (2010), i.e., by assuming that the shock surface has the three-dimensional shape of a hemispherical shell with thickness equal to the 2D projected thickness d of the WL intensity jump across the shock, corrected for the shock motion during the LASCO C2 or C3 exposure time. For each frame we estimated an average value of the shock depth L, and applied the same value to the whole shock front. Given L, and by adopting the radial density profiles derived from the analysis of the LASCO C2 pB, the shock compression ratio X can be inferred directly from the comparison between the observed and the expected total brightness ratios: $(tB_d/tB_u)_{obs} = (tB_d/tB_u)_{exp}$.

The corresponding curves for the compression ratio X measured along the shock fronts with different LASCO C2 and C3 frames are reported in Figure 6. The uncertainties in X values shown in this figure are due to the uncertainty in the identification of the exact location of the shock in C2 and C3 images (see above). The compression ratio reaches the maximum value of ~2.1 at 06:47 UT at a point that is very close to center of the shock front at that time located around a latitude of −20° S; this X value is considerably lower than the upper-limit adiabatic compression of 4 expected for a monatomic gas. In all cases, the latitudinal dependence is similar: X has a maximum around the center of the shock front, decreasing progressively but not monotonically toward the flanks. As the shock expands, the X values decrease on average along the whole of the shock fronts: for instance, at 08:09 UT the maximum value is ~1.5; as already pointed out in the previous section, this indicates that the shock is dissipating its energy while propagating in the corona. These results are in agreement with those reported by Bemporad & Mancuso (2011) in their analysis of a different CME-driven shock. We notice here that, as explained above, the X values have been derived not after background subtraction, but from the ratio between the total brightnesses observed at the shock location and those observed at the same pixels in the frame acquired just before the arrival of the shock. This method allows removal from the ratio of any possible uncertainty due to the instrumental calibration; moreover, because the shock is the faster feature propagating outward, no significant changes occurred in the corona aligned along the line of sight between the two frames other than the compression due to the shock.

The Alfvénic Mach number is defined as the ratio between the upstream plasma velocity v_u (i.e., the velocity of the plasma flowing toward the shock surface in the reference frame at rest with respect to the shock itself) and the Alfvén speed v_A, $M_A \equiv v_u/v_A$. M_A can be estimated from the compression ratio X and the angle θ_{sh} under two assumptions: (1) the plasma $\beta \ll 1$ (β is the ratio between the thermal and magnetic plasma pressures) and (2) the upstream magnetic field is radially directed, so that the angle between the shock normal and the magnetic field vector can be assumed to be equal to θ_{sh} on the plane of the sky. These are not strong assumptions, as discussed in Bemporad & Mancuso (2011), and can be considered fairly verified also in our case. Under these hypotheses, as we verified observationally in Bemporad et al. (2014) and theoretically in Bacchini et al. (2015), the Alfvénic Mach number is well approximated in the general case of oblique shock by the following semi-empirical formula:

$$M_{A\angle} = \sqrt{M_{A\parallel}^2 \cos^2\theta_{sh} + M_{A\perp}^2 \sin^2\theta_{sh}}, \tag{4}$$

where $M_{A\parallel} = \sqrt{X}$ and $M_{A\perp} = \sqrt{\frac{1}{2}X(X+5)/(4-X)}$ are the expected Mach numbers for parallel and perpendicular shocks, respectively, for a $\beta \ll 1$ plasma. The validity of Equation (4) has been confirmed by the analysis of Bemporad et al. (2014), which takes advantage of both WL and ultraviolet data from the UVCS on board *SOHO* (see discussion therein) and has been recently tested with MHD numerical simulations by Bacchini et al. (2015). This equation allowed us to derive, from different values of X and θ_{sh} parameters, 2D polar maps of $M_{A\angle}$ values, as shown in Figure 7 (top-right panel). This map clearly shows that in the early phases the shock was super-Alfvénic at all latitudes (with larger M_A values at the shock nose), while later on (i.e., higher up) it keeps super-Alfvénic numbers only at the nose.

The Alfvén speed can be derived, in turn, from M_A values once the upstream plasma velocity is known or estimated. The

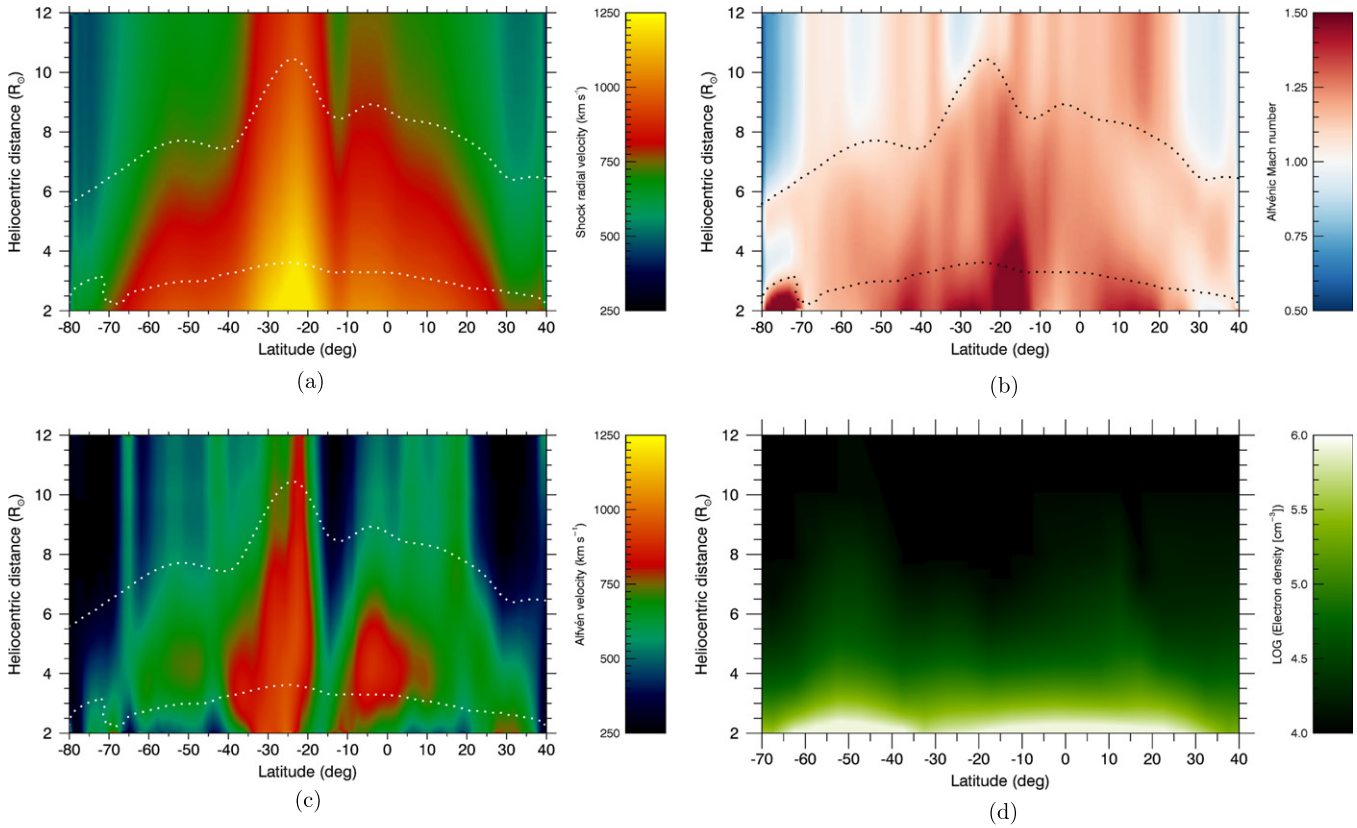

Figure 7. 2D maps showing the distribution of the radial shock velocity v_r (a), the Alfvénic Mach number M_A (b), the Alfvén speed v_A (c), and as a reference the pre-shock coronal densities n_e (d). The M_A and v_A values are derived by assuming a negligible solar wind speed, as described in the text. In each panel real measurements were obtained only in the region between the two dotted lines, while values shown outside this region have been extrapolated to higher and lower altitudes.

upstream velocity is given by $v_u = |\boldsymbol{v}_{sw} - \boldsymbol{v}_{sh}|$, where $\boldsymbol{v}_{sw}$ is the speed of the outflowing solar wind, assumed to be radial, and $\boldsymbol{v}_{sh}$ is the shock speed. In our case, we have no direct measurements of the wind flows in the corona, hence we must adopt a model for the solar wind expansion in order to infer the Alfvén speed from the Alfvénic Mach number. To this end, a first-order approximation can be obtained by assuming $\boldsymbol{v}_{sw} = 0$ in the previous equation, i.e., by neglecting the solar wind entirely. This is not a realistic assumption, but it is rather reasonable, considering that at low altitudes in the corona ($\lesssim 5\ R_\odot$) and in the early phase of propagation, the shock speed may be up to one order of magnitude larger than typical wind velocities measured outside coronal holes ($\approx$100–300 km s^{-1}; see, e.g., Susino et al. 2008). Under this hypothesis, the estimated Alfvén speed can be considered as an upper limit to the real values. Possible consequences of this assumption will be discussed in the last section.

2D polar maps of the Alfvén speed are shown in Figure 7 (bottom-left panels); these maps have been obtained again with polynomial (third-order) interpolation of the Alfvén speeds measured at different locations (i.e., latitudes and altitudes) of the shock front at different times (Figure 4). Results plotted in Figure 7 clearly show that the Alfvén speed has not only radial, but also significant latitudinal modulations. The Alfvén speed reaches the highest value ($\sim$1000 km s^{-1}) at the lowest altitudes in the equatorial belt. The latitudinal dependence is rather complex, with an alternation of local minima and maxima ranging between $\sim$600 and $\sim$1000 km s^{-1}. At increasing altitudes, v_A generally decreases, with values that never exceed 800 km s^{-1} at 12 $R_\odot$. Interestingly, the regions characterized by the slowest decrease in electron density (around $\sim$50° S and around $\sim$10° N; see Figure 3) are also those where the Alfvén speed decreases more steeply, reaching values below $\sim$500 km s^{-1} already at 5 $R_\odot$. As a consequence, in the early propagation phase (i.e., at low altitudes) the shock is significantly super-Alfvénic not only at the nose but also in several regions distributed in the flanks of the shock surface. These high-density and high-Mach number regions are very probable candidates for sources of particle acceleration and type-II radio bursts; we discuss in the next section possible correlations with the sources of radio emission identified from RDS, while the determination of the magnetic field strength is discussed in the last section.

3.2. Radio Dynamic Specrum

As is well known, shock waves are able to accelerate electron beams to suprathermal energies, which in turn can produce Langmuir waves that are converted by means of nonlinear wave–wave interactions into electromagnetic waves near the fundamental and/or harmonic of the local electron plasma frequency f_{pe}. Since the coronal density n_e decreases with increasing heliocentric distance and $f_{pe} \propto n_e^{1/2}$, the expanding shock surface produces type-II radio emissions at decreasing frequencies as it propagates through space, and the measured frequency drift rate at a given time is directly related to the shock speed. The observed frequency drift rate therefore provides information on the shock dynamics through the corona, while its onset depends on the local magnetosonic speed.

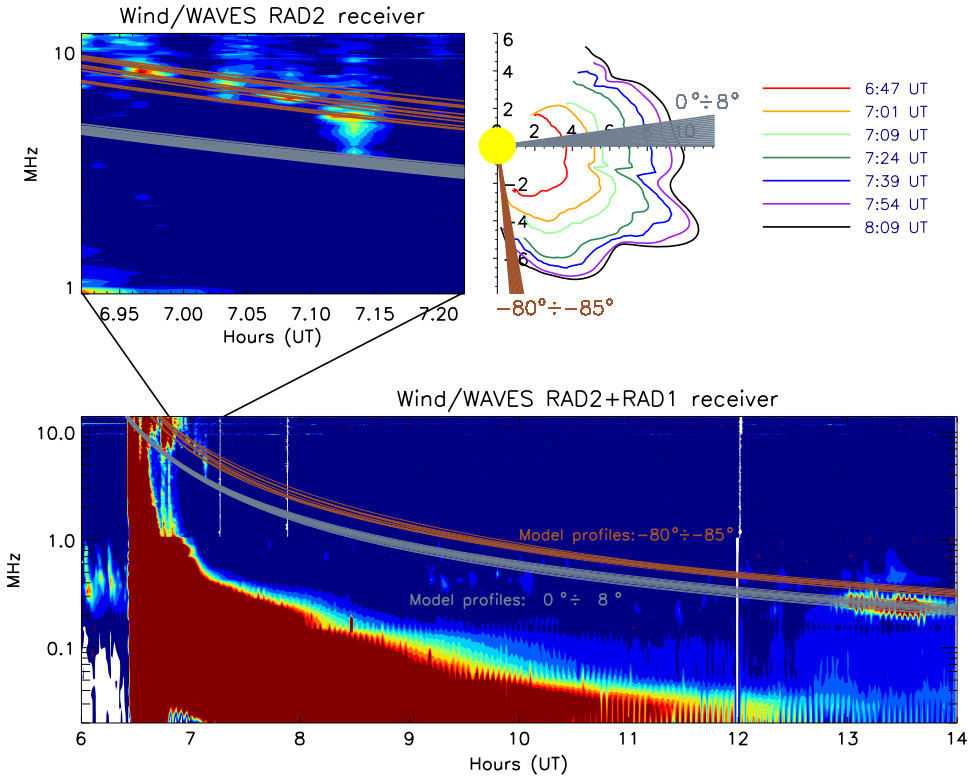

Figure 8. Lower panel: dynamic spectrum of the *Wind*/WAVES radio data in the frequency range between 20 kHz and 13.8 MHz from 6 to 14 UT on 2011 June 7, showing the decametric to kilometric type-II radio emissions associated with the CME. The upper panel at the left shows details of the radio emission associated with the emission excited earlier at the southern flank of the shock. The curves on this plot are also explained in the text.

The dynamic spectrum in the lower panel of Figure 8 shows the intensity of the radio data from 06:00 to 14:00 UT on 2011 June 7 in the frequency range between 20 kHz and 13.8 MHz measured by the RAD1 and RAD2 radio receivers of the WAVES experiment on the *Wind* spacecraft. A very intense, complex type-III-like radio emission was observed beginning at 6:24 UT. This fast-drifting radio emission can be interpreted as the first radio signature indicating the lift-off of the CME from the Sun (e.g., Reiner & Kaiser 1999) and probably originates from the reconfiguration of the magnetic field in the lower corona that allows the energetic electrons produced by the flare to escape into the interplanetary medium (Reiner et al. 2000). Two slowly drifting episodes of strong type-II emission were also observed in the decametric range around 07:00 UT (clearly visible in the expanded upper left panel of Figure 8) and after 09:00 UT, abruptly intensifying between 13:00 and 14:00 UT (lower panel of Figure 8). We interpret these bands of emissions as second harmonics, as is usually assumed when only one band is visible. The origin of the second harmonic emission in type-II bursts is well understood as a result of coalescence of two plasma waves into a transverse one at twice the plasma frequency. Less intense, additional, slowly drifting, type-II-like radio emissions at different times and frequencies are also visible, probably originating from different portions of the super-Alfvénically expanding shock surface.

In order to model the observed complex type-II radio emissions displayed in Figure 8, we need to know the coronal electron density profile at the time of the CME event. In fact, the density profile allows us to convert the height measurements related to the shock surface dynamics to corresponding values of the coronal density as the frequencies f are simply obtained as $f \approx f_{\rm pe} \approx 9\sqrt{n_{\rm e}\,[{\rm cm}^{-3}]}$ kHz. Instead of relying on a generic coronal electron density model, as is usually done in the literature, we used the coronal electron density at different heliocentric distances and latitudes provided by the LASCO pB measurements discussed in the previous section. These density estimates, obtained for heliocentric distances greater than about 2 $R_{\odot}$, correspond to radio frequencies below about 14 MHz, i.e., the range of radio emissions observed in the *Wind*/WAVES dynamic spectrum. By assuming, as usual, second harmonic type-II emission and using the coronal density distribution inferred from the available LASCO pB observations to relate the type-II frequencies to their heliocentric heights, we identified, knowing the shock's surface height from the previous analysis, a set of synthetic type-II profiles that were superimposed (as dashed lines in Figure 8) on the radio dynamic spectrum for comparison with the actual type-II emissions. This comparison allowed us to characterize all observed type-II features and, in particular, two distinct regions (assuming radial propagation) along the shock's surface where the brightest radio emissions were most likely generated. An accurate estimate of the model radio profiles could only be obtained considering the coronal parameters outward from the flare longitude of 66° W and not from 90° W (plane of sky). Unfortunately, at the time when the CME occurred, the *STEREO-A* and *-B* spacecraft were located at 94°.9 and 93°.0 from the Sun–Earth line, respectively. Hence, coronagraphic images acquired by the *STEREO* coronagraphs would not provide any useful information about the corona lying on the meridional plane at 66° W. Having said that, although we assume that no significant temporal and longitudinal variations are present between the density profile we inferred on the plane

of the sky and the density actually met by the shock, this assumption is undoubtedly much more realistic than the one that involves the adoption of a generic power-law density profile, as is usually done in the literature for studies of this kind (see, e.g., Reiner & Kaiser 1999; Pohjolainen & Lehtinen 2006; Liu et al. 2009; Kong et al. 2015).

With the above caveat in mind, we show that the two strong type-II bursts in this event are probably generated by two different portions of the shock (see upper right panel of Figure 8), one driven near the CME front and the other one at the southern flank region of the CME. We point out that the angular ranges specified in Figure 8 are not intended to designate the accuracy of our results, but that they are simply meant to illustrate the angular location of the models that better fit the observed type-II features. This result supports the scenario of type-II shock generation typically arising at the CME flank due to interaction with a nearby streamer (e.g., Mancuso & Raymond 2004; Cho et al. 2008). In this case, the type-II-emitting shock front may be quasi-perpendicular and thus apt to accelerate electrons by the shock drift acceleration mechanism (Holman & Pesses 1983).

4. DISCUSSION AND CONCLUSIONS

The actual limitations in our understanding of many physical phenomena occuring in the solar corona are due in the first place to our limited knowledge of the coronal magnetic field. Knowledge of its strength and orientation is primarily based on extrapolations from observations of magnetic fields in the photosphere, where the magnetic field is strong and the Zeeman effect produces a detectable splitting of atomic levels and a subsequent polarization of the emitted light. Nevertheless, extrapolations from photospheric fields are model-dependent, static (no eruptive events) and fail to reproduce accurately complex coronal topologies. For these reasons, many different techniques have been developed to measure magnetic fields in the extended corona using radio observations and taking advantage of Faraday rotation (e.g., Mancuso & Spangler 1999; Mancuso & Garzelli 2013a, 2013b) and circular polarization in radio bursts (e.g., Hariharan et al. 2014), or in the lower corona with EUV images using coronal seismology (e.g., West et al. 2011) and field extrapolations bounded to 3D reconstructions (e.g., Aschwanden et al. 2014). The recent development of spectro-polarimetric measurements of magnetic field strength and orientation is now providing very promising results (e.g., Tomczyk et al. 2007; Dove et al. 2011), even if (due to the required polarimetric sensitivities) these techniques can be applied only in the lower corona ($h < 0.4\ R_\odot$).

Recently, an interesting technique to measure coronal fields with CME-driven shocks was proposed by Gopalswamy & Yashiro (2011). This technique takes advantage of the relationship derived by Russell & Mulligan (2002) between the standoff distance of an interplanetary shock and the radius of curvature of its driver, and is applied to derive the strength of coronal fields just above the shock nose during its propagation. This technique has been applied to images obtained from WL coronagraphic observations and, recently, to CME-driven shocks observed with EUV disk imagers (Gopalswamy et al. 2012) and WL heliospheric images (Poomvises et al. 2012), allowing for the first time the derivation of magnetic field strengths up to a heliocentric distance of $\sim$200 $R_\odot$. Notwithstanding the above, this technique has some limitations, in particular: (1) it can be applied only to shocks driven by CMEs, and (2) it is able to provide magnetic field measurements only along the radial located at the position of the shock nose.

On the other hand, the technique we developed here and in our previous works is able to provide measurements of the pre-shock coronal magnetic field strengths from WL observations of shock waves over all altitudes and latitudes crossed by the shock, independently of any hypothesis on the nature of the shock driver. In fact, once 2D maps for the Alfvén speed and for the electron density n_e are derived, the determination of the 2D coronal magnetic field strength is straightforward and is given by $B = v_A\sqrt{4\pi n_e m_p}$. The resulting 2D map of the magnetic field strength is shown in Figure 9 (top-left panel) under the assumption that the solar wind speed is negligible with respect to the shock speed. Nevertheless, because the shock speed is decreasing with altitude ($v_{sh} \simeq 1200\ \mathrm{km\ s^{-1}}$ at 2.5 $R_\odot$ and $v_{sh} \simeq 1000\ \mathrm{km\ s^{-1}}$ at 12 $R_\odot$ as we measured at the shock center), while the wind speed is increasing, higher up in the corona the field will be more and more overestimated, leading to larger uncertainties. In order to quantify these uncertainties, lower-limit estimates for the Alfvén speed, and thus for the magnetic field, have been derived by assuming that the whole corona is pervaded at all latitudes by fast solar wind; in particular, here we assumed the radial profile of a fast solar wind provided by Hu et al. (1997). The resulting 2D map for the lower-limit estimate of the magnetic field strength is shown in Figure 9 (bottom-left panel). Comparison between the two maps clearly shows that no significant differences are present in the lower corona, while larger differences may exist higher up. In particular, by averaging all the radial profiles of magnetic field obtained at different latitudes, we conclude that the maximum difference between the upper- and the lower-limit estimates is of the order of a factor $\sim$2.7 at 12 $R_\odot$, and smaller factors at lower altitudes (see Figure 9, right panel).

The magnetic field values we derived here are in very good agreement with previous measurements provided in the literature at different altitudes and latitudes and obtained with many different techniques, as shown in Figure 10. Hence, not only is the radial variation of the field strength comparable to other estimates obtained with completely different techniques, but the latitudinal modulation we derived in this work is reliable as well. We recall that the technique applied in this work for the determination of field strengths was only based on the analysis of WL coronagraphic images, which have been analyzed to derive 2D maps (projected on the plane of the sky) of the pre-shock coronal densities, shock compression ratios, shock velocities, and inclination of the shock surface with respect to the radial. Then, some assumptions were needed in order to derive the magnetic field strengths: first, we assumed that above the lower boundary of the LASCO C2 occulter ($\sim$2 $R_\odot$) the coronal field is radial, so that the shock inclination with respect to the radial also provides its inclination with respect to the upstream magnetic field. This is not a strong assumption, because it is well known that coronal structures (outlining the magnetic field orientation) are nearly radial above heliocentric distances of $\sim$2 $R_\odot$. Second, we assumed an empirical formula for the determination of the Alfvénic Mach number for the general case of an oblique shock starting from the measured shock compression ratios and shock inclination angles. The validity of this formula has been verified in a previous work (Bemporad et al. 2014) where the Alfvénic Mach number was derived independently also from the analysis of WL and UV

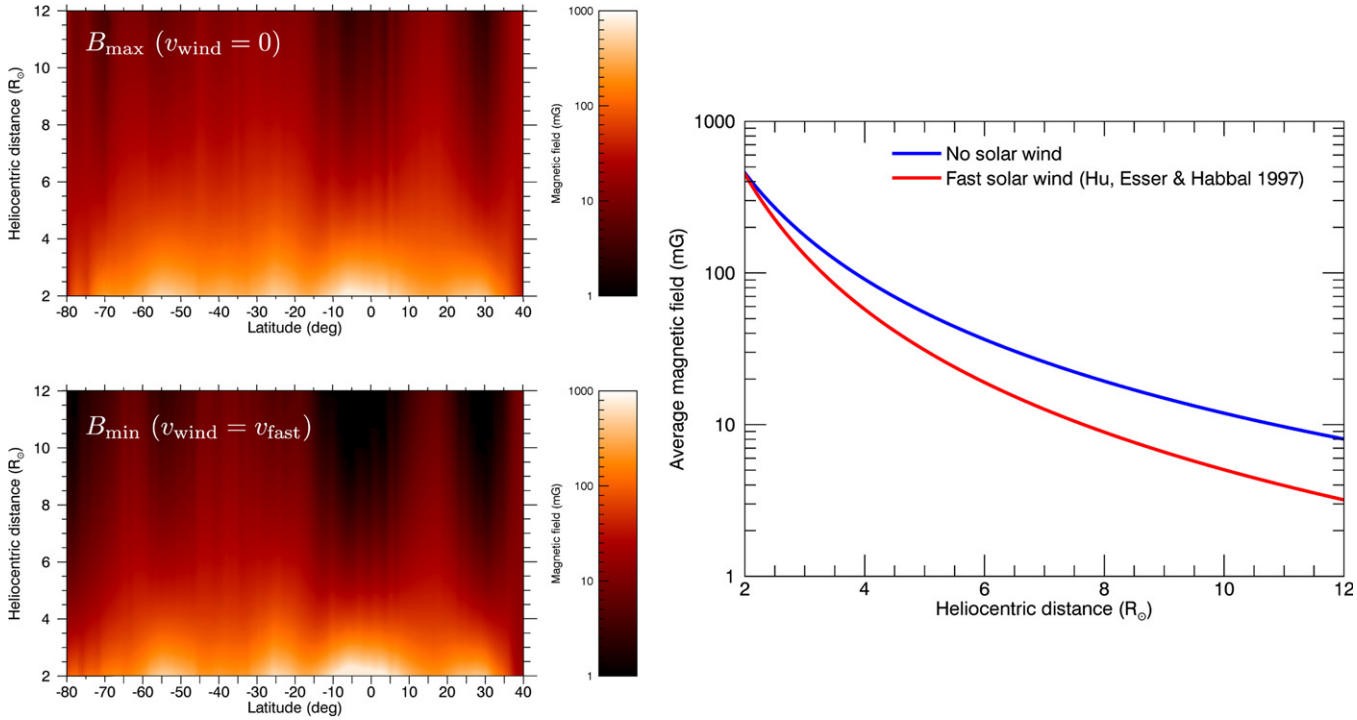

Figure 9. Comparison between the 2D maps of coronal magnetic field strengths derived by assuming negligible wind speed (top left, upper limit for the field values) and fast wind speed at all latitudes (bottom left, lower limit for the field values). The right panel shows a comparison between the latitudinal average of magnetic fields obtained under the assumption of negligible wind speed (blue line) and assuming fast wind speed at all latitudes (red line).

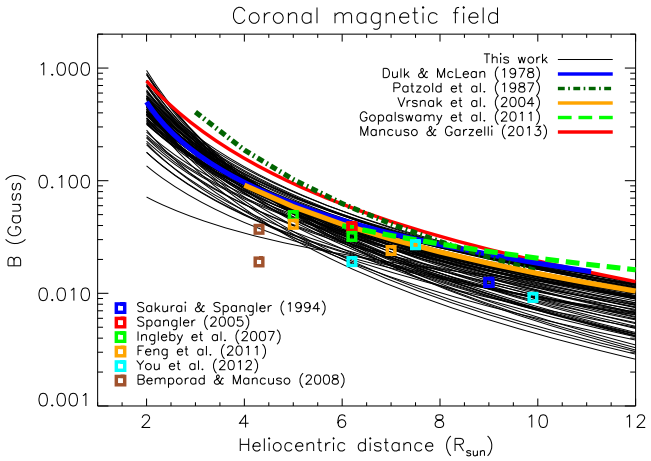

Figure 10. Comparison between radial magnetic field profiles derived in this work at different latitudes (solid black lines), other magnetic field radial profiles provided in the literature (in particular: Dulk & McLean (1978)—solid blue line, Patzold et al. (1987)—dashed-dotted dark green line, Vrsnak et al. (2004)—dashed-dotted orange line, Gopalswamy & Yashiro (2011)—dashed green line, and Mancuso & Garzelli (2013a)—solid red line) together with a compilation of other measurements (in particular: Sakurai & Spangler (1994)—blue boxes, Spangler (2005)—red boxes, Ingleby et al. (2007)—green boxes, Feng et al. (2011)—orange boxes, You et al. (2012)—cyan boxes, and Bemporad & Mancuso (2010)—brown boxes).

data; the verification of the same formula with MHD numerical simulations has also recently been provided by another work (Bacchini et al. 2015). Third, in order to convert the derived Alfvénic Mach numbers in estimates for the Alfvén speed, we assumed that the solar wind speed ahead of the shock is negligible with respect to the shock speed; as discussed above, this leads to an overestimate of the magnetic field by a factor of no more than ∼2.7 at 12 $R_\odot$, decreasing with altitude. For comparison with the WL coronal structures, the magnetic field values derived in this work are shown again in Figure 11, plotted in the field of view of the LASCO C2 coronagraph (right panel), together with the original pre-CME coronal WL intensity (left panel). We also notice that the latitudinal distribution of coronal field strength is, to a first approximation, anticorrelated with the WL intensity. This result is also better shown in Figure 12, providing the latitudinal distribution of the normalized WL intensity and the magnetic field strength at a constant altitude of 2.75 $R_\odot$. The observed anticorrelation is in nice agreement with what we could expect around the vertical axis of each coronal streamer, where the neutral current sheet corresponds to a region of minimum magnetic field strength.

In order to further support the correctness of our measurements of coronal magnetic fields, we also applied the same technique proposed by Gopalswamy & Yashiro (2011) and based on the measurement of the shock standoff distance. In order to perform the comparison between the two techniques, we selected the LASCO C2 frame where the circular shape of the CME flux rope is better visible, shown in Figure 13. For this frame we determined the position of the center of the flux rope (plus symbol in the left plot) and (looking at previous and subsequent frames) the CME propagation direction (dashed line in the left plot). This provides us with the identification of the shock nose, as well as a measurement of the sum of the shock standoff distance Δ and the radius R of the flux rope, which turns out to be $\Delta + R = 1.48\ R_\odot$. We thus used the value of the Mach number derived as decribed above at the

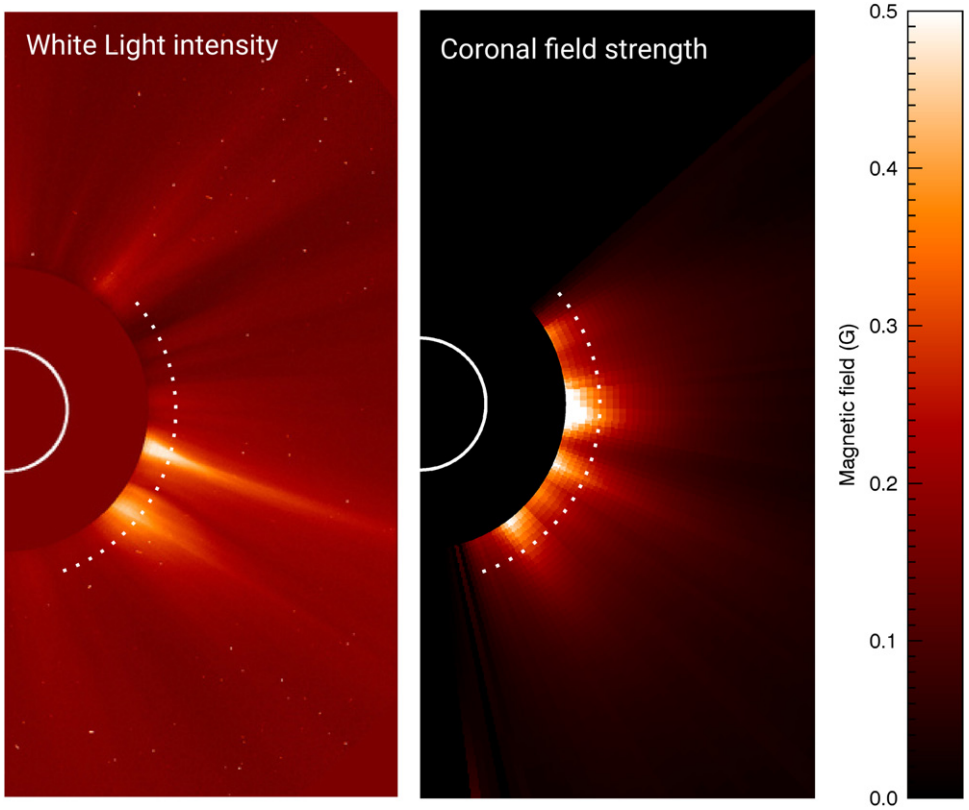

Figure 11. Comparison between the pre-shock coronal white light structures observed by the LASCO C2 coronagraph (left) and the magnetic field strengths derived in this work in the LASCO C2 field of view (right). The dashed lines show the location where latitudinal profiles of the WL intensity and field strength have been extracted to be plotted in Figure 12.

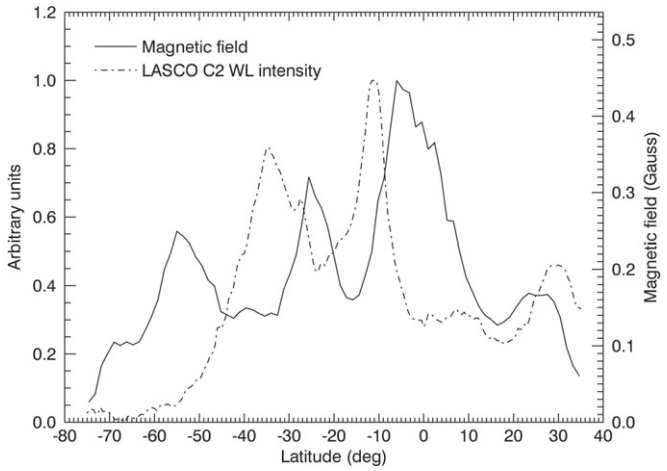

Figure 12. Comparison between the normalized pre-shock coronal white light structures observed by the LASCO C2 coronagraph (dashed line) and the magnetic field strengths (solid line) at the constant altitude of 2.75 $R_{\odot}$.

shock nose ($M_A = 1.50$) and derived the expected Δ/R ratio, which turns out to be (see Gopalswamy & Yashiro 2011)

$$\frac{\Delta}{R} = K\frac{(\gamma - 1)\, M_{\rm A}^2 + 2}{(\gamma + 1)\, M_{\rm A}^2} \simeq 0.45, \qquad (5)$$

where $K = 0.78$ for a circular shape of the shock driver, and $\gamma = 5/3$. With the above numbers it turns out that $\Delta = 0.46$ $R_{\odot}$ and $R = 1.02$ $R_{\odot}$. The corresponding circumference (plotted in the left panel of Figure 13) shows a quite nice agreement with the location of the CME flux rope, thus demonstrating that our results are in good agreement with those that could be derived for the same event with the technique described by Gopalswamy & Yashiro (2011). Moreover, since in this work we derived measurements of the shock Mach number $M_{\rm A}$ not only at the shock nose but also at different latitudes, it is interesting to test what happens by assuming that the above relationship relating $M_{\rm A}$ and the Δ/R ratio also holds away from the shock nose. In particular, the right plot of Figure 13 shows the locations of the shock driver (black dotted line) as inferred by assuming different values of $M_{\rm A}$ away from the shock nose along each radial starting from the same position of the center of the flux rope (plus symbol). The resulting curve shows a surprisingly nice agreement with some WL features visible between the CME flux rope and shock. This may suggest that at this time a decoupling between the flux rope and the shock is already occurring away from the shock nose, or alternatively that the side parts of the shock are driven at some latitudes by the expansion of other loop-like plasma features surrounding the CME flux rope and embedded within the same CME.

The analysis performed here provides not only a new technique to derive coronal field strengths with unprecedented radial and latitudinal extent, but also very important insights into the physical relation between the type-II emitting regions and the shock front. In fact, the difference between the 2D maps we derived for the shock and the Alfvén speed clearly shows that in the early phases (2–4 $R_{\odot}$) the whole shock surface is super-Alfvénic, while later on (i.e., higher up) it

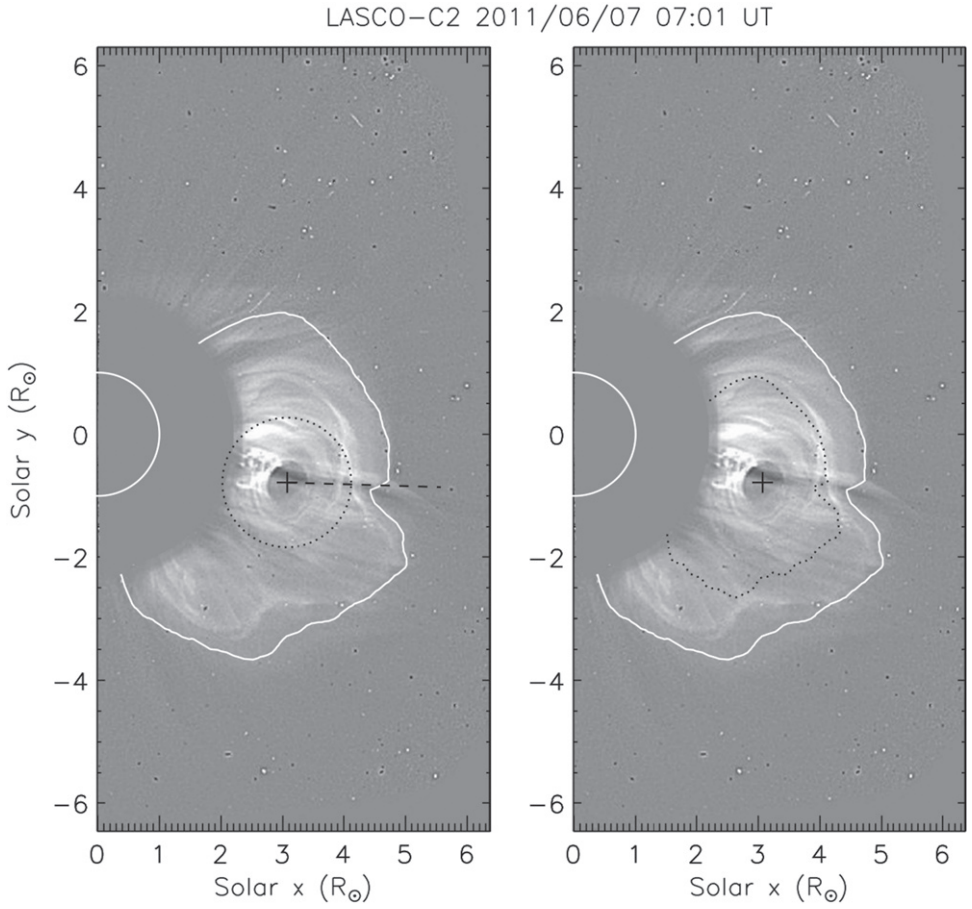

Figure 13. Left: LASCO C2 base-difference image acquired on 2011 June 7 at 07:01 UT and with the contrast of faint features enhanced using the filter provided by the JHelioviewer software. The overplot shows the location of the shock (solid white line), the center of the CME flux rope (plus symbol), and the CME propagation direction (dashed black line). Right: same frame as shown in the left panel, where the overplot provides again the location of the shock (solid white line), the center of the CME flux rope (plus symbol), and the location of the shock driver (black dotted line) as derived by assuming that the relationship between the Mach number at the shock nose and the Δ/R ratio holds also at different latitudes away from the shock nose (see text).

becomes super-Alfvénic only at the nose. For a better understanding of the acceleration regions of SEPs, this result has also to be considered together with our previous finding that in the early propagation phases shocks are supercritical only at the nose and become subcritical later on (e.g., Bemporad & Mancuso 2011). At the same time, we demonstrate here with analysis of RDS that the emission near the front was generated later than that produced by the flanks, in agreement with the conclusion we derived from the analysis of WL data. This suggests that the acceleration of SEPs leading to gradual events could also involve at different times coronal regions located not only at different altitudes but also at different latitudes and/or longitudes along the shock front, as recently simulated for instance by Rodríguez-Gasén et al. (2014).

REFERENCES

Ackermann, M., Ajello, M., Albert, A., et al. 2014, ApJ, 787, 15
Antonucci, E. 2006, SSRv, 124, 35
Aschwanden, M. J., Sun, X., & Liu, Y. 2014, ApJ, 785, 34
Bacchini, F., Susino, R., Bemporad, A., & Lapenta, G. 2015, ApJ, 809, 58
Bemporad, A., & Mancuso, S. 2010, ApJ, 720, 130
Bemporad, A., & Mancuso, S. 2011, ApJL, 739, L64
Bemporad, A., & Mancuso, S. 2013, JAdR, 4, 287
Bemporad, A., Susino, R., & Lapenta, G. 2014, ApJ, 784, 102
Billings, D. E. 1966, A Guide to the Solar Corona (New York: Academic)
Carlyle, J., Williams, D. R., van Driel-Gesztelyi, L., et al. 2014, ApJ, 782, 87
Chen, Y., Du, G., Feng, L., et al. 2014, ApJ, 787, 59
Cheng, X., Zhang, J., Olmedo, O., et al. 2012, ApJL, 75, L5
Cho, K.-S., Bong, S.-C., Kim, Y.-H., et al. 2008, A&A, 491, 873
Cho, K.-S., Gopalswamy, N., Kwon, R.-Y., et al. 2013, ApJ, 765, 148
Classen, H. T., & Aurass, H. 2008, A&A, 384, 1098
Dolei, S., Bemporad, A., & Spadaro, D. 2014, A&A, 562, A74
Dorovskyy, V. V., Melnik, V. M., Konovalenko, O. O., et al. 2015, SoPh, 290, 2031
Dove, J. B., Gibson, S. E., Rachmeler, L. A., et al. 2011, ApJL, 731, L1
Dulk, G. A., & McLean, D. J. 1978, SoPh, 57, 279
Eselevich, M. V., & Eselevich, V. G. 2011, ARep, 55, 359
Eselevich, V., & Eselevich, M. 2012, ApJ, 761, 68
Feng, S. W., Chen, Y., Li, B., et al. 2011, SoPh, 272, 119
Gilbert, H. R., Inglis, A. R., Mays, M. L., et al. 2013, ApJL, 776, L12
Gopalswamy, N., Mäkelä, P., Akiyama, S., et al. 2012, JGR, 117, A08106
Gopalswamy, N., Nitta, N., Akiyama, S., et al. 2012, ApJ, 744, 72
Gopalswamy, N., Xie, H., Mäkela, P., et al. 2013, AdSpR, 51, 1981
Gopalswamy, N., & Yashiro, S. 2011, ApJL, 736, L17
Hariharan, K., Ramesh, R., Kishore, P., Kathiravan, C., & Gopalswamy, N. 2014, ApJ, 795, 14
Hayes, A. P., Vourlidas, A., & Howard, R. A. 2001, ApJ, 548, 1081
Hess, P., & Zhang, J. 2014, ApJ, 792, 49
Holman, G. D., & Pesses, M. E. 1983, ApJ, 267, 837
Hu, Y. Q., Esser, R., & Habbal, S. R. 1997, JGR, 102, 14661
Ingleby, L. D., Spangler, S. R., & Whiting, C. A. 2007, ApJ, 668, 520
Inglis, A. R., & Gilbert, H. R. 2013, ApJ, 777, 30
Innes, D. E., Cameron, R. H., Fletcher, L., et al. 2012, A&A, 540, L10
Jin, M., Manchester, W. B., van der Holst, B., et al. 2013, ApJ, 773, 50
Kohl, J. L., Noci, G., Cranmer, S. R., & Raymond, J. C. 2006, A&ARv, 13, 31
Kong, X., Chen, Y., Guo, F., et al. 2015, ApJ, 798, 81

Kouloumvakos, A., Patsourakos, S., Hillaris, A., et al. 2014, SoPh, 289, 2123
Li, T., Zhang, J., Yang, S., & Liu, W. 2012, ApJL, 746, L13
Liu, Y., Luhmann, J. G., Bale, S. D., & Lin, R. P. 2009, ApJL, 691, L151
Liu, Y. C.-M., Opher, M., Wang, Y., & Gombosi, T. I. 2011, A&A, 527, A46
Magdalenić, J., Marqué, C., Krupar, V., et al. 2014, ApJ, 791, 115
Manchester, W. B., van der Holst, B., Tóth, G., & Gombosi, T. I. 2012, ApJ, 756, 81
Mancuso, S., & Garzelli, M. V. 2013a, A&A, 553, A100
Mancuso, S., & Garzelli, M. V. 2013b, A&A, 560, LL1
Mancuso, S., & Raymond, J. C. 2004, A&A, 413, 363
Mancuso, S., & Spangler, S. R. 1999, ApJ, 525, 195
Minnaert, M. 1930, ZA, 1, 209
Mujiber Rahman, A., Shanmugaraju, A., Umapathy, S., & Moon, Y.-J. 2013, JASTP, 105, 181
Ontiveros, V., & Vourlidas, A. 2009, ApJ, 693, 267
Patzold, M., Bird, M. K., Volland, H., et al. 1987, SoPh, 109, 91
Pohjolainen, S., & Lehtinen, N. J. 2006, A&A, 449, 359
Poomvises, W., Gopalswamy, N., Yashiro, S., et al. 2012, ApJ, 758, 118
Reale, F., Orlando, S., Testa, P., et al. 2013, Sci, 341, 251
Reale, F., Orlando, S., Testa, P., et al. 2014, ApJL, 797, L5
Reiner, M. J., & Kaiser, M. L. 1999, GeoRL, 26, 397
Reiner, M. J., Karlický, M., Jiricka, K., et al. 2000, ApJ, 530, 1049
Reiner, M. J., Vourlidas, A., Cyr, O. C., St., et al. 2003, ApJ, 590, 533
Rodríguez-Gasén, R., Aran, A., Sanahuja, B., et al. 2014, SoPh, 289, 1745
Russell, R. T., & Mulligan, T. 2002, P&SS, 50, 527
Sakurai, T., & Spangler, S. R. 1994, ApJ, 434, 773
Schwenn, R. 2006, LRSP, 3, 2
Spangler, S. R. 2005, SSRv, 121, 189
Susino, R., Ventura, R., Spadaro, D., Vourlidas, A., & Landi, E. 2008, A&A, 488, 303
Tomczyk, S., McIntosh, S. W., Keil, S. L., et al. 2007, Sci, 317, 1192
van de Hulst, H. C. 1950, BAN, 11, 135
van Driel-Gesztelyi, L., Baker, D., Török, T., et al. 2014, ApJ, 788, 85
Vourlidas, A., Subramanian, P., Dere, K. P., & Howard, R. A. 2000, ApJ, 534, 456
Vourlidas, A., Wu, S. T., Wang, A. H., et al. 2003, ApJ, 598, 1392
Vršnak, B., & Cliver, E. W. 2008, SoPh, 253, 215
Vrsnak, B., Magdalenic, J., & Zlobec, P. 2004, A&A, 413, 753
West, M. J., Zhukov, A. N., Dolla, L., & Rodriguez, L. 2011, ApJ, 730, 122
Williams, D. R., Baker, D., & van Driel-Gesztelyi, L. 2013, ApJ, 764, 165
You, X. P., Coles, W. A., Hobbs, G. B., & Manchester, R. N. 2012, MNRAS, 422, 1160